The effect of carbonate mineral additions on biogeochemical conditions in surface sediments and benthic-pelagic exchange fluxes

Kadir Bice[1,*,~], Tristen Myers[2,#], George Waldbusser[2], Christof Meile[1,*]

[1] Department of Marine Sciences, University of Georgia, Athens GA 30602

[2] College of Earth, Ocean, and Atmospheric Sciences, Oregon State University, Corvallis, OR 97331

[#] now at: Pacific Northwest National Laboratory, Sequim, WA 98382

[~] now at: Department of Civil and Environmental Engineering, Massachusetts Institute of Technology, Cambridge, MA 02139

Correspondence to: Kadir Bice (bicekadir@gmail.com), Christof Meile (cmeile@uga.edu)

Abstract. Coastal sediments are hotspots of biogeochemical processes that are impacting subsurface and overlying water conditions. Fluid composition in sediments is altered through the mineralization of organic matter which under oxic conditions, further lowers both pH and the carbonate saturation state. As a potential mitigation strategy for this sediment acidification, we explored the effects of mineral additions to coastal sediments. We experimentally quantified carbonate mineral dissolution kinetics of carbonate shells suitable for field application, and then integrated this data into a reactive transport model that represents early diagenetic cycling of C, O, N, S and Fe, and traces total alkalinity, pH and saturation state of $CaCO_3$. Model simulations were carried out to delineate the impact of mineral type and amount added, porewater mixing and organic matter mineralization rates on sediment alkalinity and its flux to the overlying water. Model results showed that the added minerals undergo initial rapid dissolution and generate saturated conditions demonstrating the potential of alkalinity enhancement in mitigating surface sediment acidification. Aragonite dissolution led to higher total alkalinity concentrations than calcite. Simulations of carbonate mineral additions to sediment environments with low rates of organic matter mineralization exhibited a substantial increase in mineral saturation state compared to sediments with high CO_2 production rates, highlighting the environment-specific extent of the effect of mineral addition. Our work indicates that carbonate additions have the potential to effectively buffer surficial sediments over multiple years, yielding biogeochemical conditions that counteract the detrimental effect of low pH sediment conditions on larval recruitment, and potentially increase benthic alkalinity fluxes to support marine carbon dioxide removal (mCDR) in the overlying water.

1. Introduction

In coastal systems, ocean-freshwater mixing, terrestrial inputs, and active biogeochemical transformations (Cai et al., 2017; Soetaert et al., 2007) lead to natural fluctuations in pH that are large and decoupled from the decrease in pH observed in the open ocean due to ocean acidification (Hofmann et al., 2011). Especially in shallow water environments, sediments play a significant role as benthic fluxes can constitute a substantial alkalinity source to the overlying water, increasing its buffering

capacity (Rassmann et al., 2016; Krumins et al., 2013; Cyronak et al., 2013b). Sediments receive organic matter (OM) from the overlying water which fuels the dissolution of carbonate minerals and early diagenetic processes. Aerobic respiration and other processes consuming dissolved O_2 can lead to steep pH decreases within the oxygenated sediment and the interaction of

35   OM mineralization and mineral dissolution determines the balance of the porewater carbonate system (Burdige et al., 2010; Jourabchi et al., 2005). Mineral dissolution and early diagenesis are connected through the changes in carbonate system which impacts mineral saturation states and hence the rate of dissolution (e.g., Morse et al., 2007). Apart from its impact on mineral dissolution, OM mineralization is also a significant contributor to alkalinity generation under suboxic and anoxic conditions (Hu & Cai, 2011a). These early diagenetic processes determine the composition of the porewaters, which affect benthic

40   calcifying organisms; furthermore, they can affect the biogeochemical conditions in the overlying water through benthic fluxes releasing nutrients and alkalinity.

In surface sediments, porewater pH is generally lower than in the overlying water, in particular when sediment O_2 uptake is elevated due to burrowing and irrigation activities by benthic macrofauna (e.g. Aller, 1982). This exposes benthic organisms that live in the upper layers of the sediment to more corrosive conditions (Green et al., 2013; Waldbusser & Salisbury, 2014).

45   Combined with abundant OM, enhanced supply of O_2 into the sediment also leads to elevated fluxes of alkalinity and DIC to the water column (Mucci et al., 2000; Burdige et al., 2007).

In this study, we investigate the effects of the addition of carbonate minerals in the coastal sediments focusing on benthic alkalinity generation and release in a shallow water environment. Such ocean alkalinity enhancement (OAE) aims to buffer increased dissolved CO_2 in the ocean by dissolving carbonate or silicate minerals, producing alkalinity. OAE is mainly studied

50   for its effect on ocean - atmosphere CO_2 exchange, the impact on organisms (Renforth & Henderson, 2017) and its potential to mitigate ocean acidification and lower atmospheric CO_2 concentrations (marine carbon dioxide removal; mCDR). Previous studies have shown that increasing ocean alkalinity through enhanced weathering has the potential to reverse global ocean acidification in an intermediate CO_2 emission scenario (RCP 4.5) and reduce its impacts if emissions were to continue to rise throughout the 21st century (RCP 8.5) (Taylor et al., 2016). To date, OAE implementations mainly target the open ocean and

55   are aimed at identifying the potential of scaling up the mCDR efforts to a global scale (Fennel et al., 2023). Recent studies also focused on the impact of OAE on marine ecosystems such as fish and plankton communities (Goldenberg et al., 2024; Paul et al., 2024; Ferderer et al., 2022). Only a few studies focused on coastal OAE and even fewer on sedimentary applications (Green et al., 2009, 2013; Hangx et al., 2009; Fuhr et al., 2024), where the effectiveness of OAE mainly depends on the dissolution rate of the mineral which is controlled by the mineral and the chemistry of the water and physical properties of the environment

60   (Hartmann et al., 2013; Montserrat et al., 2017). One benefit of implementing OAE in coastal sediments is the generally higher rate of organic matter remineralization. This elevated CO_2 generation aids mineral dissolution, given most overlying marine waters are typically super-saturated with respect to carbonate minerals. Here, we simulate this effect of adding carbonate minerals to the sediment using a reactive transport model. We use measurements of carbonate mineral dissolution rates to assess the extent and duration of buffering in surficial sediments, and the impact on benthic alkalinity fluxes. Building on the

65 previous work by Krumins et al. (2013) that explored the interaction of carbonate chemistry with early diagenesis in coastal sediments, our work identifies factors that determine the impact of sediment alkalinization on the spatial and temporal distribution of buffering by exploring the effect of mineral type, amount, organic matter remineralization rate and bioturbation.

2. Methods

2.1. Dissolution experiments

70 Dissolution rates for the minerals used in this model were derived from lab-based experiments detailed in Myers (2022). We provide pertinent details below. Two biomineral calcium carbonates, calcitic oyster shells *Crassostrea gigas* (below referred to as "bio-calcite") and aragonitic clam soft-shell clam shells, *Mya arenaria,* ("bio-aragonite") were collected from Oregon Oyster Farm in Newport, Oregon, USA and from Broad Cove in Yarmouth, Maine, USA, respectively. The biomineral samples were briefly cleaned, dried, crushed and sieved through a 2000 µm sieve and retained on 710 µm, for an approximately median

75 grain size of 1 mm. We measured the mineral dissolution rate across four saturation states experimentally; $\Omega_{calcite} = 0.25$ (low), 0.45 (mid), 0.85 (hi) and 1.03 (saturated); carbonate chemistry conditions are detailed in Table S1. A flow-through, feedback-controlled with pH monitoring and CO_2 injection seawater system similar to Waldbusser et al. (2011) was used for manipulations at the Hatfield Marine Science Center (HMSC), Newport, OR, USA (additional details in Myers, 2022). pH measurements from each manipulation tank were compared against a benchtop meter daily during the experiment. pH was

80 additionally compared against a reference sample in which pCO_2 and TCO_2, in situ temperature and salinity were measured to calculate pH on the NBS scale. pH (all tanks) and temperature (low and pre-treatment tanks) data were recorded every ten minutes. The coefficient of determination (R^2) between measured benchtop pH data and the pH data calculated from pCO_2/TCO_2 measurements for header tanks in all experiments was consistently greater than 0.9 across all experiments (Figure S2). Plug-flow style dissolution chambers were 2.5 cm ID, 12.7 cm long, schedule 40 PVC pipe, with 150 µm Nitex mesh on

85 either end of the upright chambers. Approximately 50 ($\pm$ 0.1) grams of biomineral were used in each chamber, water was initially added slowly and agitated to remove air bubbles prior to initiating flow. Flowrates were controlled to 17 ($\pm$ 1.2) mL min^{-1} and experiments were run for three to four days to verify consistent alkalinity concentrations, as observed in trials conducted to optimize the experiment (Myers, 2022). Using the inlet and outlet measured alkalinity concentrations from an individual chamber (mol alkalinity L^{-1}), the measured flow rate (L d^{-1}), and the known amount of sample added (g$_{mineral}$), the

90 change in alkalinity in mol alkalinity g$_{mineral}^{-1}$ d^{-1} was recorded as (Eq. 1):

$$\Delta = \frac{([alkalinity]_{outlet} - [alkalinity]_{inlet})}{(mineral\ amount)} * flow\ rate$$

The early diagenetic model (see below) uses a rate law in which the volumetric dissolution rate R_d (in mol$_{mineral}$ m$^{-3}_{sediment}$ d^{-1}) depends on the concentration of the mineral (mol$_{mineral}$ m$^{-3}_{sediment}$), the saturation state Ω (= ion concentration product/solubility

95 K_{sp}) and the dissolution rate constant k_d (d^{-1}) (Jourabchi et al., 2008):

$$R_d = k_d[Mineral](1 - \Omega)^n \tag{2}$$

In the experiment, the dissolving mineral is the entire solid phase, so that $g_{mineral} = g_{solid\ phase}$. Hence, the mineral concentration in $mol_{mineral}/g_{solid\ phase}$ is the molecular weight of the mineral ($MW_{mineral}$) and k_d can be calculated from the measured Δ as:

$$k_d = \frac{\Delta\ *\ MW_{mineral}}{\frac{dTA}{dR}\ *\ (1-\ \Omega)^n} \tag{3}$$

where dTA/dR is the mineral to alkalinity stoichiometric ratio in the dissolution reaction ($+2\ mol_{alkalinity}/mol_{mineral}$; Table 3) and n is the rate order.

2.2. Carbonate Chemistry Measurements

Alkalinity

Open-cell alkalinity titrations were conducted over the course of the experiment, utilizing a two-point titration after Edmond (1970), as modified by Waldbusser et al. (2011). A micrometer burette was used with a micro pH probe with precisions of 0.002 mL and $\pm$ 0.02, respectively. The probe was calibrated with NBS calibration standards (pH = 4, 7, and 10) daily before being used to take measurements. As outlined in Waldbusser et al. (2011), Baker Analyzed Reagent grade 0.0995-0.1005 normal HCl acid was used as the titrant with reagent grade NaCl to a final molar concentration of 0.7 to minimize gap junction potentials during titrations. Analytical precision and accuracy were compared against triplicate titrations and Dickson CRM batch 142, respectively, and found to have an average coefficient of variance of 0.07% and typically ±16 µmol or less, for precision and accuracy.

Dissolved Inorganic Carbon, pCO2, and Carbonate Calculations

pCO_2/TCO_2 samples were collected in clean amber glass ~350 ml bottles preserved with 30 microliters of saturated $HgCl_2$ and sealed with polyurethane-lined crimp-sealed metal caps. Analysis via the Burkalator was carried out to measure pCO_2 and TCO_2 via near-infrared detection following the procedure of Bandstra et al. (2006), modified for discrete samples as in Hales et al. (2005), Barton et al. (2012), and Hales et al. (2017). Liquid and gas standards were employed to ensure the accuracy of pCO_2/TCO_2 measurements. The system can resolve the accuracy and precision of TCO_2 concentrations within $\pm$ 0.02% and 2% for pCO_2 (Hales et al., 2017). Carbonate chemistry parameters were calculated using dissociation constants from Millero (2010). Salinity was measured on the sample bottles following pCO_2/TCO_2 measurements via a salinometer (8400B "Autosal" Laboratory Salinometer; Guildline Instruments, Sorrento, FL, US). Calculated carbonate chemistry variables presented in association with the mineral dissolution experiments were computed using CO2calc and the K_1 and K_2 carbonic acid dissociation constants from Lueker et al. (2000), K_{HSO4} constants from Dickson et al. (1990), sulfate constants from Morris & Riley (1966), fluorine constants from Riley (1965), and boron constants from Uppström (1974).

2.3. Reactive transport modeling

A one-dimensional diagenetic model was developed to simulate the distribution of chemical species with depth in the sediment over time. The model domain extended 20 cm deep into the sediment discretized into 50 intervals with a linearly increasing grid size of 1 mm at the top and 1 cm at the bottom. The model included 13 state variables, representing chemicals involved in the main early diagenetic reactions, and mineral dissolution/precipitation (Table 1). At the upper boundary, the

concentrations of solutes and fluxes of solids were imposed, while at the bottom boundary, no gradient conditions were imposed for all chemicals.

Table 1: State variables and their upper boundary conditions. Seawater compositions are computed with *aquaenv* (Hofmann et al. 2010) for the pressure, temperature and salinity given in Table 2.

Variable	Notation	Boundary condition
Oxygen	O_2	0.2 mM
Sulfate	SO_4^{2-}	Seawater composition
Total sulfide	TS	0 mM
Dissolved inorganic carbon	DIC	equilibrium with a given alkalinity and pH 7.96
Total alkalinity	TA	1.9 mEq/L (measured at Yaquina Bay)
Calcium	Ca^{2+}	Seawater composition
Magnesium	Mg^{2+}	Seawater composition
Iron	Fe^{2+}	0 mM
Ammonium	NH_4^+	0 mM
Nitrate	NO_3^-	0.02 mM
Carbonate mineral (s)	$CaCO_3$	$F = 0$ µmol cm^{-2} yr^{-1}
Iron oxides (s)	$Fe(OH)_3$	$F = 1$ µmol cm^{-2} yr^{-1}
Iron sulfide (s)	FeS	$F = 0$ µmol cm^{-2} yr^{-1}

The spatio-temporal evolution of the concentrations was described by an advection-diffusion equation with the addition of bioturbation and bioirrigation and the effect of reactions. Bioturbation was treated as a diffusive process (Boudreau, 1997) and bioirrigation was described as a non-local exchange between porewater at depth and the overlying water (Boudreau, 1984). The governing equations were:

$$\phi \frac{\partial C_i}{\partial t} = -\frac{\partial \phi u C_i}{\partial x} + \frac{\partial}{\partial x}\left(\phi(D_i + D_b)\frac{\partial C_i}{\partial x}\right) + \sum_r s_{ir} R_r + B_i \tag{4}$$

$$(1-\phi)\frac{\partial C_j}{\partial t} = -\frac{\partial (1-\phi)v C_j}{\partial x} + \frac{\partial}{\partial x}\left((1-\phi)D_b\frac{\partial C_j}{\partial x}\right) + \sum_r s_{jr} R_r \tag{5}$$

where t is time, x is depth in sediment, ϕ is porosity, C_i (C_j) is the concentration of the solute i (in mol/volume pore fluid; solid j in mol/volume solid phase), u is the burial velocity for solutes (v for solids), D_i is the diffusion coefficient of the solute i, D_b is the depth bioturbation coefficient, R_r is the rate of production/consumption through reaction r (in mass/total volume and time), s is the stoichiometric coefficient for solute i or solid j in reaction r and B_i represents bioirrigation for solute i.

Porosity is constant with time but depth-dependent and exponentially decreases with depth reflecting steady state sediment compaction (Eqn. 6):

$$\phi_x = \phi_\infty + (\phi_0 - \phi_\infty)e^{-\frac{x}{\gamma}} \tag{6}$$

where ϕ_∞ and ϕ_0 are the porosities at infinite depth and at the top of the sediment, respectively, and γ is the e-folding distance for the porosity. Burial velocities were corrected for compaction (Berner, 1980):

$$u_x = v_\infty \frac{\phi_\infty}{\phi} \tag{7}$$

$$v_x = v_\infty \frac{(1 - \phi_\infty)}{(1 - \phi)} \tag{8}$$

Diffusion coefficients were calculated using the R package *marelac* after Boudreau (1997) at a given salinity, temperature and pressure (Soetaert et al., 2010) and corrected for tortuosity (Boudreau, 1996) so that:

$$D_i = \frac{D_{aq,i}}{1 - 2ln(\phi_x)} \tag{9}$$

where D_{aq} is the molecular diffusion coefficient of solute i in solution. The bioturbation coefficient decreases exponentially with depth below the mixed layer,

$$D_b = D_{b0}e^{-\max(0,\ x - x_m)} \tag{10}$$

where x_m is the depth of mixed layer and D_{b0} is the bioturbation coefficient at the SWI, calculated as a function of water depth (Middelburg, 1997).

Bioirrigation is defined as an exchange between the surface layer and deeper layers of the sediment which was constrained by a bioirrigation coefficient exponentially decreasing with depth:

$$B_x = \alpha_0 e^{(-\frac{x}{\varepsilon})}\phi_x\left(C_{i,0} - C_{i,x}\right) \tag{11}$$

where α_0 is the bioirrigation coefficient at the SWI, ε is the e-folding distance for bioirrigation and $C_{i,x}$ is the concentration of solute i at depth x.

Table 2: Environmental parameters

Parameter	Value
Salinity	35
Temperature	12 deg C
Overlying water pH(total)	7.96
Pressure	1.013 bar
Seawater density	1.027 kg L^{-1}
Sediment density	2.65 g cm^{-3} (Boudreau, 1997)
Porosity decay with depth (γ)	5 cm (Rooze et al., 2016)
Porosity at the surface (ϕ_0)	0.8
Porosity at infinite depth (ϕ_∞)	0.6
Sedimentation at infinite depth (v_∞)	0.5 cm yr^{-1} (Middelburg, 1997)

Bioturbation mixing coefficient at the top (D_{b0})	30 cm^2 yr^{-1} (Middelburg, 1997, water depth <5m)
Bioturbation e-folding distance	1 cm (Soetaert et al., 1996)
Depth of mixed layer (x_m)	4 cm (Rooze et al., 2016)
Bioirrigation rate constant at the top (α_0)	200 yr^{-1} (Wang & Cappellen, 1996; Meile & Cappellen, 2003)
Bioirrigation decay with depth (ε)	3.5 cm (Thullner et al., 2009)

165

Reactions considered in the model include organic matter mineralization with aerobic and anaerobic pathways, reoxidation of reduced species and mineral formation/dissolution reactions (Table 3). Each reaction has an impact on the total alkalinity (TA), which were taken from previous studies (Wolf-Gladrow et al., 2007; Dickson, 1981).

Organic matter is mineralized using O_2, NO_3^-, iron (oxyhydr)oxides (FeOx) and SO_4^{2-} as terminal electron acceptors and

170 modeled with Monod kinetics. The OM mineralization rate (R_C^0) was adjusted to yield a TA flux of ~1200 µmol cm^{-2} yr^{-1}. This value was chosen to match open core top incubations measured in Yaquina Bay (Myers, 2022), with the resulting R_C^0 value being comparable to earlier measurements by D'Andrea & DeWitt (2009) (~200-460 µmol C cm^{-3} yr^{-1}), and higher than values reported for deeper coastal environments (Wang & Van Capellen, 1996; Krumins et al., 2013). Reactions considered further include nitrification, iron oxidation, sulfide oxidation with O_2 and FeOx, and iron sulfide oxidation, as well as the

175 formation/dissolution of $CaCO_3$ minerals and FeS (Table 3). Following Rooze et al. (2020), at each time step, DIC is speciated to calculate CO_3^{2-} concentration and pH from DIC and alkalinity, assuming seawater concentrations of borate and negligible contributions of phosphate, silicic acid, nitrite and hydrogen fluoride and other acids or bases.

Table 3: Reactions included in the model. Benthic primary production is assumed to be negligible and organic matter has

180 Redfield stoichiometry (a = 1, b = 16/106, c = 1/106). Alkalinity production or consumption in each reaction is determined following Wolf-Gladrow et al. (2007). The total mineralization rate is defined as $R_C= R_C^0$ *exp(-x/γ_{om}) after Wang & Cappellen (1996) where γ_{om} is e-folding distance for OM mineralization.

Reaction	dTA/dR	dDIC/dR	Reaction rate
Organic Matter Mineralization			
(CH$_2$O)$_a$(NH$_3$)$_b$(H$_3$PO$_4$)$_c$ + a O$_2$ => a CO$_2$ + b NH$_4^+$ + c HPO$_4^{2-}$ + (-b+2c) H$^+$ + a H$_2$O	b - c	a	$$R_{O_2}^m = RC\,[O_2]\,/\,(K_{O_2}^m + [O_2])$$
(CH$_2$O)$_a$(NH$_3$)$_b$(H$_3$PO$_4$)$_c$ + 4a/5 NO$_3^-$ + (4a/5 +b -2c) H$^+$ => a CO$_2$ + b NH$_4^+$ + c	4a/5 + b - c	a	$$R_{NO_3}^m = \left(RC - R_{O_2}^m\right)[NO_3]\,/\,(K_{NO_3}^m + [NO_3])$$

HPO_4^{2-} + 2a/5 N_2 + 7a/5 H_2O			
$(CH_2O)_a(NH_3)_b(H_3PO_4)_c$ + 4a $Fe(OH)_3$ + (8a+b-2c) H^+ => a CO_2 + b NH_4^+ + c HPO_4^{2-} + 4a Fe^{2+} + 11a H_2O	b - c + 2*4a	a	$$R_{FeOx}^m = \left(RC - R_{O_2}^m - R_{NO_3}^m\right)[FeOx] / (K_{FeOx}^m + [FeOx])$$
$(CH_2O)_a(NH_3)_b(H_3PO_4)_c$ + a/2 SO_4^{2-} + (a/2 +b -2c) H^+ => a CO_2 + b NH_4^+ + c HPO_4^{2-} + a/2 HS^- + a H_2O	b - c + a	a	$$R_{SO_4}^m = \left(RC - RC_{O_2}^m - R_{NO_3}^m - R_{FeOx}^m\right)[SO_4] / (K_{SO_4}^m + [SO_4])$$
Secondary reactions			
NH_4^+ + 2O_2 => NO_3^- + 2H^+ + H_2O	-2	0	$$R_{NH_4}^o = k_{NH_4}^o[NH_4][O_2]$$
Fe^{2+} + 5/2 H_2O + 1/4 O_2 => $Fe(OH)_3$ + 2H^+	-2	0	$$R_{Fe}^o = k_{Fe}^o[Fe^{2+}][O_2]$$
HS^- + 2O_2 => SO_4^{2-} + H^+	-2	0	$$R_{TS}^o = k_{TS}^o[TS][O_2]$$
HS^- + 8$Fe(OH)_3$ + 15H^+ => SO_4^{2-} + 8Fe^{2+} + 20H_2O	+14	0	$$R_{TS}^{of} = k_{TS}^{of}[TS][FeOx]$$
FeS + 2O_2 => Fe^{2+} + SO_4^{2-}	0	0	$$R_{FeS}^o = k_{FeS}^o[FeS][O_2]$$
Mineral precipitation/dissolution			
FeS + 2H^+ <=> Fe^{2+} + 2HS^-	+2 (dis)/-2 (prec)	0	$$\Omega_{FeS} = [Fe][TS]/([H^+]K_{FeS}^{sp}\rho_{sw}^2)$$ $$R_{FeS} = \begin{cases} k_{FeS}^f(\Omega_{FeS} - 1), & \text{if } \Omega_{FeS} \geq 1 \\ k_{FeS}^d[FeS](1 - \Omega_{FeS}), & \text{if } \Omega_{fes} < 1 \end{cases}$$
$CaCO_3$ <=> Ca^{2+} + CO_3^{2-}	+2 (dis)/-2 (prec)	+1 (dis)/-1 (prec)	$$\Omega_M = [Ca^{2+}][CO_3]/(K_M^{sp}\rho_{sw}^2)$$ $$R_M = \begin{cases} k_M^f(\Omega_M - 1), & \text{if } \Omega_M \geq 1 \\ k_M^d[Mineral](1 - \Omega_M)^n, & \text{if } \Omega_M < 1 \end{cases}$$

Table 4: Reaction constants. Carbonate dissolution rate constants determined experimentally in this study are described in the results.

Reaction parameters	Value	Source
R_C^0	400 µmol C cm^{-3} yr^{-1}	Calibrated to match experimental TA data
γ_{om}	5 cm	(Wang & Capellen, 1996)
$K_{O_2}^m$	0.02 mM	(Rooze et al., 2016)
$K_{NO_3}^m$	0.004 mM	(Rooze et al., 2016)
K_{FeOx}^m	130 mM	(Rooze et al., 2016)
$K_{SO_4}^m$	1.6 mM	(Rooze et al., 2016)
$k_{NH_4}^o$	5000 mM^{-1} yr^{-1}	(Rooze et al., 2016)
k_{Fe}^o	140 000 mM^{-1} yr^{-1}	(Rooze et al., 2016)
k_{TS}^o	160 mM^{-1} yr^{-1}	(Rooze et al., 2016)
k_{TS}^{of}	6 mM^{-1} yr^{-1}	(Rooze et al., 2016)
k_{FeS}^o	300 mM^{-1} yr^{-1}	(Rooze et al., 2016)
K_{FeS}^{sp}	10$^{-2.2}$ (mol/kg)^2	Wang & Van Capellen (1996)
k_{FeS}^f	6*10^{-6} mol g^{-1} yr^{-1}	Wang & Van Capellen (1996)
k_{FeS}^d	10^{-3} yr^{-1}	Wang & Van Capellen (1996)
$K_{calcite}^{sp}$	4.31*10^{-7} (mol/kg)^2	f(salinity) (Mucci et al., 1983)
$K_{aragonite}^{sp}$	6.82*10^{-7} (mol/kg)^2	f(salinity) (Mucci et al., 1983)
k_M^f(calcite)	10^4 mM yr^{-1}	(Luff & Wallman, 2003)
k_M^f(aragonite)	10^5 mM yr^{-1}	(Luff & Wallman, 2003)
k_M^d (calcite)	5 yr^{-1}	(this study)
k_M^d (aragonite)	5.2 yr^{-1}	(this study)

Application

To establish initial conditions, each simulation was first run to steady state with a zero-deposition flux of calcium carbonate. After that, 8 or 16 weight % (weight of mineral/ total weight of the sediment) $CaCO_3$ were added to the top 2 cm of sediment, representing the sudden, one-time addition of the buffering carbonate minerals.. To assess the magnitude and temporal evolution of the impact of the alkalinization experiment on sediment biogeochemistry and benthic fluxes, transient simulations using these new initial conditions were then carried out, covering periods of up to 50 years.

We tested the impact of several environmental factors on the buffering effect of carbonate mineral additions to surficial sediments in comparison to the baseline addition scenario (Table 5). Specifically, we lowered the overlying water pH from 7.96 to 7.8, representing the impact of ocean acidification. The depth of the bioturbated layer affects the distribution of minerals added, which may impact the effectiveness of the extent of buffering; it was varied from the relatively shallow mixing depth of 4cm in the baseline implementation to the global average depth of bioturbation of 10 cm (Boudreau, 1997). We also varied the deposition flux of iron (oxy)hydroxides from 1 to 10 μmol/cm^2/yr to assess differences between sites that vary in the extent of coupling between Fe, S and C cycles. And as the rate of organic matter mineralization has a major impact on sediment redox conditions and porewater composition, R_C^0 was varied from the baseline value of 400 to 200 μmol/cm^3/yr to represent environments with different O_2 penetration depths. Finally, simulations were carried out to assess the impact of the type of mineral in the system (calcite vs. aragonite). The spin-up simulations were specific to each model run, and as such represent the environmental conditions (e.g., high vs. low rate of mineralization, or a setting in which either aragonite or calcite are the only carbonate mineral considered).

Table 5. Sensitivity analyses. Rows represent the scenario tested. Columns show the parameters changed.

Scenario/Parameter	R_c^0 (μmol/cm^3/yr)	Fe(OH)$_3$ flux (μmol/cm^2/yr)	Depth of mixed layer (cm)	Mineral type	pH in overlying water
Baseline	400	1	4	Calcite	7.96
Low OW pH	400	1	4	Calcite	7.8
High ML	400	1	10	Calcite	7.96
High Fe Flux	400	10	4	Calcite	7.96
Low R_c^0	200	1	4	Calcite	7.96
Aragonite	400	1	4	Aragonite	7.96

CO$_2$ drawdown

We estimated the potential impact of enhanced sediment TA fluxes on atmospheric CO_2 uptake in an enclosed bay using a simple box model. Water exchange is due to the tides, and riverine impact was assumed negligible, reflecting for example, the strong coupling of Yaquina Bay with the coastal ocean (Brown & Ozretich, 2007).

To estimate the order of magnitude of the impact of mineral additions on CO_2 uptake, we used a simple mass balance approach similar to Brenner et al. (2016), which focuses on the ratio of DIC over TA as the controlling factor of CO_2 uptake (Egleston et al., 2010). We calculated the mass balance for TA and DIC prior to and 2 years after the mineral addition and attribute the difference in atmospheric CO_2 exchange to the mineral addition. As described in detail in the Supplementary Information, we first estimated tidal water exchange from water level measurements. The characteristics of the inflowing marine (alkalinity =

2.2 mmol L^{-1}, pH = 8.0) and outflowing bay water (alkalinity = 1.9 mmol L^{-1}, pH = 7.96) were chosen to be representative of a coastal setting such as Yaquina Bay and were informed by unpublished temperature, salinity, and pH data (pers. comm. G.

220 Waldbusser). Combined with our modeled benthic exchange fluxes, this allowed us to estimate the alkalinity production in the water column (R_{TA}; Eq. 12). At steady state, the alkalinity balance is given by:

$$F_i^{TA} - F_o^{TA} + F_b^{TA} + R^{TA} = 0 \qquad (12)$$

where F_i^{TA} is the tidal influx of TA as a function of water exchange rate and oceanic TA ($F_i^{TA} = v[TA_{ocean}]$), F_o^{TA} is the tidal outflux of TA from the Bay to the ocean as a function of tidal velocity and TA of the study site ($F_o^{TA} = v[TA_{site}]$), F_b^{TA} is the

225 benthic flux computed by the reactive transport model and R^{TA} is the areal net rate of water column TA production/consumption resulting from primary productivity and respiration.

Next, we used the alkalinity and pH to calculate the DIC and converted the net alkalinity production rate into net DIC production in the water column, assuming Redfield stoichiometry. This finally allowed us to estimate the CO$_2$ exchange flux (F_a^{DIC}) necessary to close the DIC mass balance for benthic fluxes with and without mineral additions to quantify its effect on

230 ocean CO$_2$ uptake.

The mass balance for DIC is given by:

$$F_i^{DIC} - F_o^{DIC} + F_b^{DIC} + F_a^{DIC} + R^{DIC} = 0 \qquad (13)$$

where F_i^{DIC} is the tide-driven influx of DIC ($F_i^{DIC} = v[DIC_{ocean}]$), F_o^{DIC} is the outflux of DIC ($F_o^{DIC} = v[DIC_{bay}]$), F_b^{DIC} is the benthic flux of DIC, F_a^{DIC} is the atmospheric CO$_2$ uptake (negative values indicate outgassing) and R^{DIC} is the net areal reaction

235 rate producing/consuming DIC.

3. Results & Discussion

3.1. Mineral Dissolution Rates

Dissolution rates of minerals were highest under highly undersaturated conditions (Figure 1). For a given mineral saturation

240 state, bio-aragonite dissolved slightly faster than bio-calcite. Dissolution rates are approximately proportional to the degree of saturation. Thus, the dissolution rate constant k_d for each mineral was estimated using Eqns. (1) and (2) with a dissolution order (n) of 1. Kinetic constant for aragonite dissolution was previously reported as 5 yr^{-1} (Luff & Wallmann, 2003) which was comparable to the 5.2 yr^{-1} derived from our measurements. For n =1, Jourabchi et al. (2005), reported a dissolution rate constant of 3.65 yr^{-1} while our estimation for bio-calcite was 5 yr^{-1}. The results are in line with previous data synthesis studies

245 focused on mineral dissolution (Morse et al., 2007; Jourabchi et al., 2005; 2008). Acknowledging the large variability in mineral dissolution dynamics (especially *n)* in previous studies (Adkins et al., 2021; Subhas et al., 2018) making it difficult to parameterize dissolution process, we have taken *n* as 1 which provided a better fit to our shell dissolution rates.
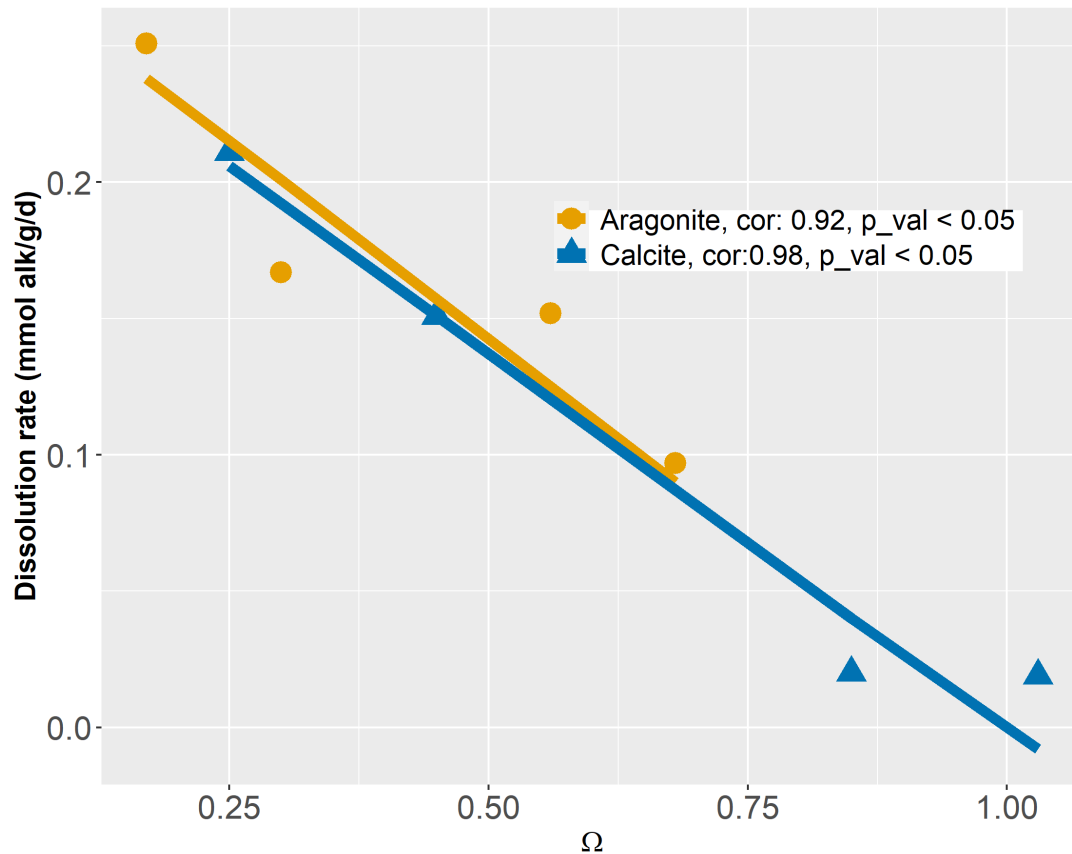
Figure 1: Saturation state for aragonite and calcite vs. their respective dissolution rates (mmol alk/g_{solid}/d). Lines show the fit
with n=1. Cor: correlation between data and the fitted line. p_val: statistical significance of the fit.

3.2. Early Diagenetic Modeling

To assess the impact of sediment alkalinization through the addition of carbonate minerals to the sediment, early diagenetic
model simulations were carried out that describe the spatio-temporal distribution of porewater and solid phase constituents.
Prior to the addition of minerals, the simulated porewater profiles show sequential depletion of electron acceptors with depth,
with O_2, NO_3^- and reactive FeOx only present in the top 5 cm (solid lines in Figure 2). SO_4^{2-} is present throughout the depth
range and only decreases by about 2.5 mM. As a result of mineralization reactions, the concentrations of reduced porewater
constituents (TS, NH_4^+, Fe^{2+}) increase with depth (Figure 2). Reduced dissolved iron (Fe^{2+}) peaked around 1 cm then decreased
with depth due to the precipitation of FeS, which in our baseline simulation limited the build-up of hydrogen sulfide (TS) and
dissolved reduced iron (Fe^{2+}). These porewater profiles reflect the sequential use of electron acceptors in the mineralization of
organic matter, through aerobic respiration and anaerobic pathways such as denitrification, dissimilatory iron and sulfate

reduction. The dominant OM mineralization pathway was SO_4^{2-} reduction (78.9%) followed by aerobic mineralization (17.2%), denitrification (3.9%) and iron reduction (0.06%).

265   DIC and TA show pronounced concentration increases with depth, reflecting OM mineralization (Figure 2 i,j). The pH profile exhibits a rapid decrease in the top centimeter to about 7, showing the impact of CO_2 production without the concurrent consumption of protons through aerobic mineralization (Table 3; Jahnke et al., 1994; Green et al., 2013). Below the oxic layer, active anaerobic OM mineralization pathways such as iron and sulfate reduction can generate considerable amounts of TA if the reaction products are not oxidized (Thomas et al., 2009). This was observed in the buildup of reduced species such as TS

270   (discussed below) which limited the drop in pH and increased saturation state (from 0.5 to > 0.8) in the deeper layers of the sediment (Figure 2 k,l). pH values were in the lower part of the range reported in Krumins et al. (2013), reflecting the lack of carbonates buffering the pH prior to the mineral additions. Sulfate reduction produced the majority of the TA and DIC (Figure 3), consistent with the findings of Krumins et al. (2013), Brenner et al. (2016) and Gimenez (2018). Aerobic mineralization produced considerable amounts of DIC in line with previous work (Thamdrup & Canfield, 2000) while generating less TA

275   than anaerobic processes and mineral dissolution (Figure 3), leading to a low porewater pH (Soetaert et al., 2007; Hofman et al., 2011). DIC and TA production by denitrification and in particular dissimilatory iron reduction was substantially less. With a high dTA/dR value (Table 3), TS oxidation with FeOx also contributed to alkalinity production. Consumption of TA was dominated by secondary redox reactions that oxidize reduced species with O_2. Due to fast kinetics, Fe^{2+} oxidation with O_2, nitrification and precipitation of FeS were the major TA consuming reactions. Brenner et al. (2016) identified sulfide oxidation

280   and nitrification as the dominant alkalinity consuming processes in the shallow water sediments in Southern North Sea. This discrepancy may be due to the potentially substantial impact of sulfide oxidation on alkalinity dynamics in organically rich near shore sediments (Krumins et al. 2013). The oxidation of reduced products of organic matter mineralization such as ammonium, hydrogen sulfide and dissolved Fe^{2+} with O_2 all lower alkalinity, albeit using different amounts of molecular oxygen. However, the oxidation of hydrogen sulfide with iron oxide as electron donor produces a large amount of alkalinity,

285   that either accumulates if the reduced iron produces is captured in the sediment or is removed if the Fe^{2+} subsequently reacts with O_2 in the oxic zone (see Table 3). Coupling of SO_4^{2-} reduction with FeS precipitation has been shown to be an important mechanism for TA burial on continental shelves (Gustafsson et al., 2019). However, in our simulations, FeS formation was limited by Fe availability, which led to the buildup of hydrogen sulfide in the porewater.

Effect of carbonate mineral additions

290   After adding carbonate minerals, the concentration profiles of primary redox species largely remained unchanged (Figure 2). This is because the organic matter mineralization rate expressions (Table 3) do not contain dependencies on the carbonate system or pH, as is common in early diagenetic models (e.g., Jourabchi et al., 2008; Morse & Mackenzie, 1990). Mineral addition slightly decreased Fe^{2+} while increasing FeS concentrations. This is due to TA production due to carbonate dissolution, which elevates the pH and increases the saturation state of FeS (Table 3), promoting FeS formation which eventually can lead

295   to the long term removal of reduced sulfur through pyrite burial (Hu & Cai, 2011a)

The added carbonate minerals started to dissolve in our model, producing 1 DIC and 2 TA per carbon (Burdige et al., 2010; Zeebe & Wolf-Gladrow, 2001), so that both the pH (Figure 2k) and porewater saturation state (Figures 2l and 4B) initially increased (Cai et al., 2011). After 2 years, CO_2 production still lowered pH in the oxic layer and prevented full saturation. However, Ω was always above 0.9 and reached 1 at and below a depth of approximately 2.5 cm and subsequent decrease was observed below 12 cm.. Following the addition of carbonates, the extent of the undersaturated conditions was constrained to the top 2 cm only, while in the natural buffering scenario reported in Krumins et al. (2013) porewater remained undersaturated in the top 10 cm. This demonstrates the potential of OAE in mitigating surface sediment acidification and providing potential benefits for calcifiers living in the upper sediment layers. As mineral addition counteracts porewater acidification, it generates biogeochemical conditions conducive for the survival of juvenile bivalves.

300
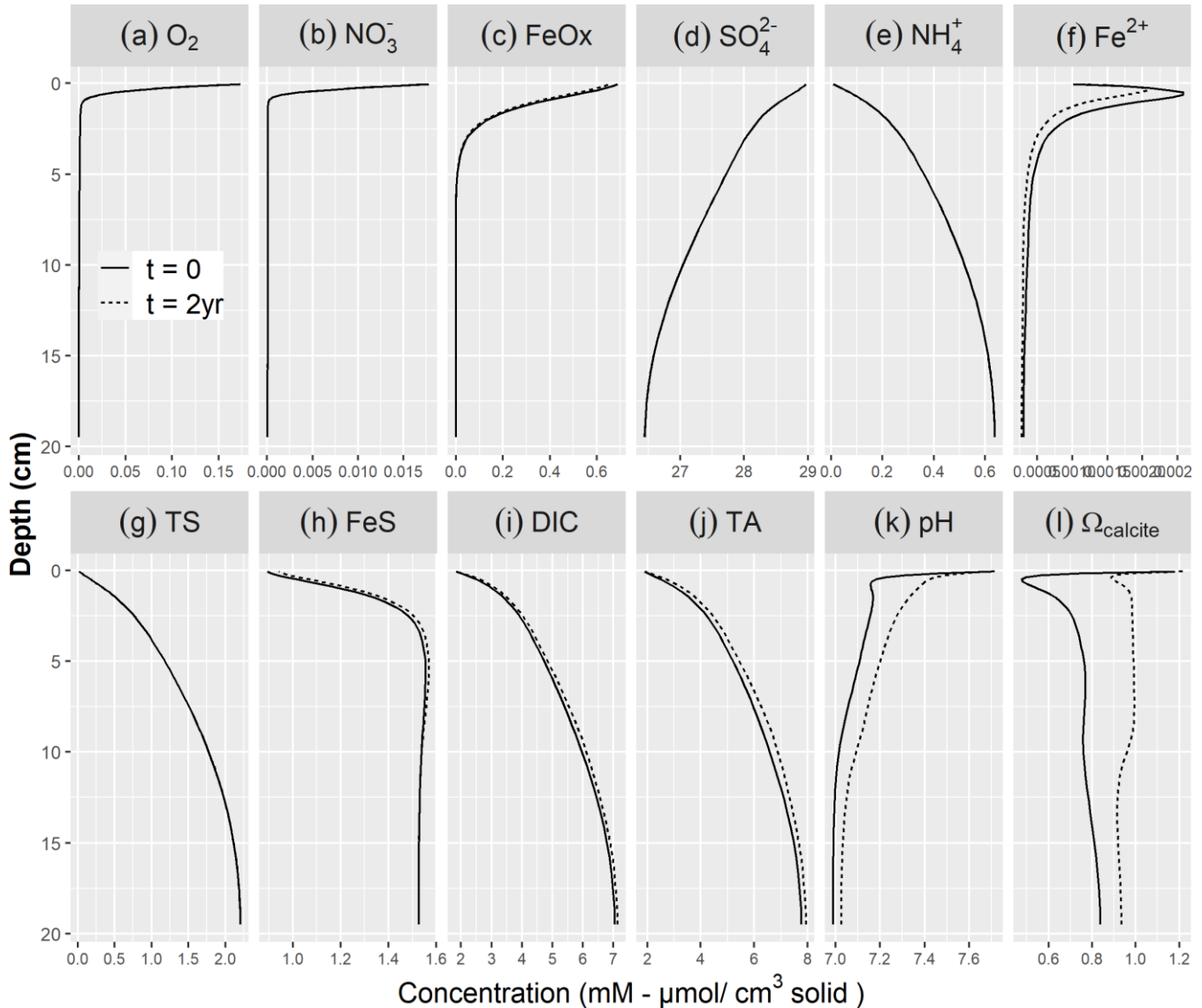
305

Figure 2. Simulated baseline porewater profiles of (a) O_2, (b) NO_3^-, (c) FeOx, (d) SO_4^{2-}, (e) NH_4^+, (f) Fe^{2+}, (g) TS, (h) FeS, (i) DIC, (j) TA, (k) pH and (l) $\Omega_{calcite}$ with 8% calcite addition. The solid lines denote the steady state profiles prior to the addition of calcite to the top 2 cm, while the dashed line indicate the simulated profiles 2 years after the mineral addition (some are coinciding with the solid lines and hence not visible). Dissolved constituents are in mmol/L porewater, while solids are given in μmol/cm^3 solid phase.

Our results are in line with literature showing that the main alkalinity producing processes were calcite mineral dissolution, sulfate reduction, denitrification and sulfide oxidation with iron oxides (Krumins et al., 2013; Berelson et al., 2007). Although organic matter mineralization reactions generate alkalinity, they have lower dTA/dDIC ratios than mineral dissolution on a per carbon basis (Table 3), and the TA producing mineralization reactions are mostly coupled to TA consuming reoxidation reactions. Therefore, the net effect of (some) mineralization pathways on TA production can be limited (Krumins et al., 2013). For example, the amount of TA generated by benthic denitrification was almost balanced out by NH_4^+ oxidation (Figure 3) which results in the small effect of N cycling on alkalinity. This is in line with previous studies showing strong coupling between oxidation/reduction of N in the marine environment (Middelburg et al., 1996) and its weak impact on buffering capacity of the overlying water (Hu & Cai, 2011b). Since reoxidation reactions are dependent on the availability of O_2, enhanced biological mixing can also increase TA consumption as previously demonstrated by Rao et al. (2014) for Fe^{2+} oxidation by O_2. Although total production of TA was around 1300 μmol cm^{-2} yr^{-1} (Figure 3, baseline with bio-calcite), total TA fluxes from bio-calcite were slightly lower, which points to the importance of consumption of TA in the oxic layer as previously reported in Krumins et al. (2013). Finally, before mineral addition, we observed a small production of calcite at the top of the sediment due to oversaturated conditions in overlying water. After the addition however, added mineral dissolved in deeper layers which led to net dissolution and generation of alkalinity in the sediment column.
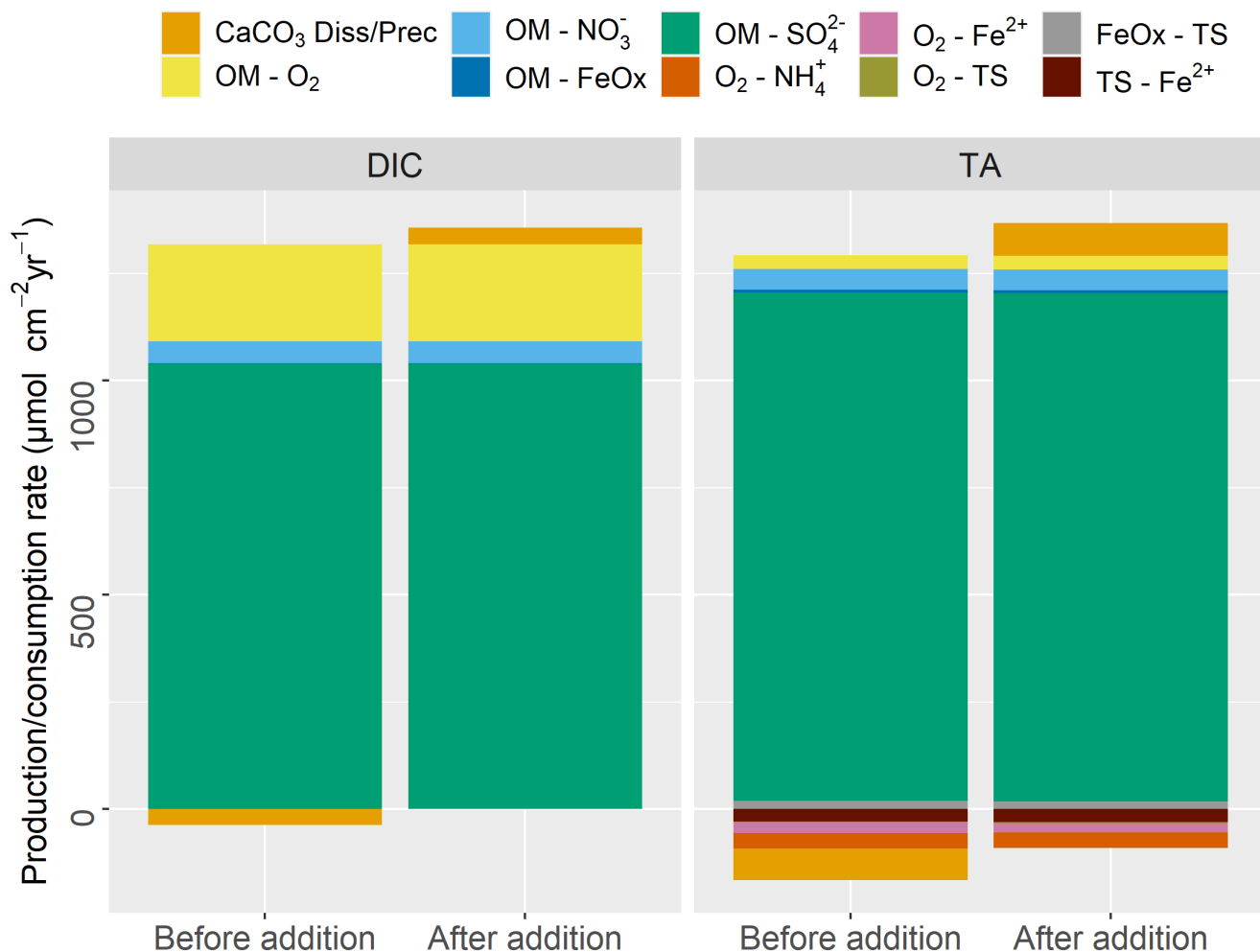
Figure 3. DIC and TA production (positive) and consumption (negative) by different early diagenetic processes integrated over the entire model domain for steady state (t = 0; before addition) and 2 years after the addition.

330

Temporal evolution of buffering with different minerals and amounts

Longer-term simulations (50 yrs) were performed to investigate the evolution of the buffering with time, considering different amounts and types of minerals added. We focused on the biogeochemical conditions in the top 10 cm of sediment, because the surficial sediment is most relevant for juvenile bivalves impacted by acidification. Figure 4 shows the temporal evolution of

335   TA and saturation state following the addition of minerals to the steady state conditions at t=0. Depth-averaged TA concentrations in top 10 cm peaked around the 2nd year after addition, with a significant drop starting around year 10 for the 8% mineral addition and around year 15 for the 16% addition and then return to steady state levels after more than 30 years

(Figure 4A). Doubling the amount of mineral added generated slightly higher TA and extended the length of the peak buffering period. The simulation of aragonite addition produced higher alkalinity concentrations than that of calcite by approximately 0.3 mM at the peak time reflecting its higher solubility. However, TA levels in aragonite application dropped faster after approximately 10 and 15 yrs and approached the initial pre-mineral application levels after about 30 and 40 years, for 8% and 16% additions, respectively. In contrast, following the addition of calcite, TA concentrations remained elevated over longer time periods. Averaging over 4 cm yielded the same patterns (with slightly lower TA concentrations) as shown in Figure 4 (not shown).
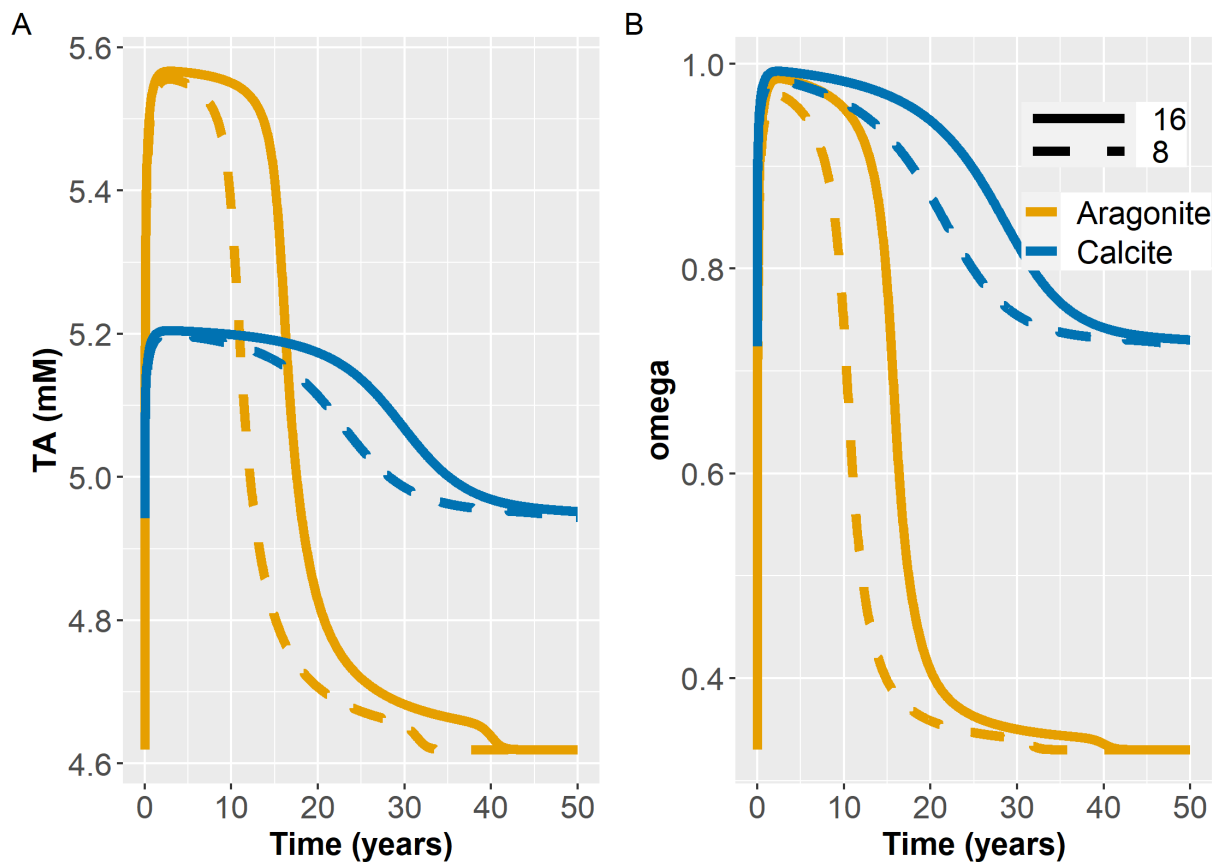
Figure 4. Temporal evolution of depth-averaged TA after addition of bio-aragonite and bio-calcite (A), and saturation states (B) in baseline simulation. Concentrations and saturation states are averaged over the top 10 cm of sediment. Colors show the type of mineral added. Solid and dashed lines show the addition of 16% and 8% respectively.

Being less stable than calcite, aragonite had a slightly faster dissolution rate constant and a larger solubility product (Burdige et al., 2010). Therefore, it generated higher TA concentrations and benthic fluxes early on. Because of its higher solubility, it initially took aragonite slightly longer to reach saturation than calcite (i.e., orange curve reaches maximum slightly after the blue one). As the rate of dissolution is set to be proportional not only to the degree of undersaturation but also the carbonate mineral concentration (Eq. 2), doubling the mineral addition had a more pronounced effect for aragonite which was approaching saturation more slowly than calcite (Figure 4B). Burial of carbonate minerals below 10 cm led to a faster decrease in TA in aragonite due to its higher dissolution. Initial conditions in 50 years simulations with calcite had higher saturation state than aragonite implementation therefore, after the impact of addition got buried, calcite levelled at higher saturation state and TA than aragonite.

Sensitivity analyses

The impact of mineral additions on the generation of alkalinity depends not only on the type of mineral added, but also on which early diagenetic processes dominate (Figure 3). The relative magnitude of these processes depends on a number of factors, including the rate of organic matter mineralization, the extent of bioturbation, the deposition fluxes of potential electron acceptors such as iron oxyhydroxides, and the composition of the overlying water. Varying these factors in our model, we explore their impact on both the environmental conditions in the surficial sediment as well as the impact on benthic alkalinity fluxes.

In our simulations, under all scenarios, mineral saturation states reached similar values at the end of the 2 years with a low R_C^0 scenario generating the highest values (blue dots in Figure 5A). However, saturation was reached fastest in the deeper mixed layer scenario which then decreased by years 1 and 2. Baseline, high FeOx flux and low R_C^0 scenarios showed a similar time course, while the addition of aragonite instead of calcite exhibited the slowest increase in saturation state (Figure 5A). Depth-averaged TA concentrations were highest following the addition of aragonite (Figure 5B). Deepening the bioturbation layer did not have much of an impact, the high FeOx flux scenario produced slightly lower TA than the baseline and the lowest amounts of alkalinity were produced by the low R_C^0 scenario. pH increased the most and fastest in the aragonite implementation, followed by low R_C^0 conditions (Figure 5C). Although the deep mixed layer scenario increased pH faster than the baseline and high FeOx flux scenarios, these three scenarios converged to a similar pH as the impact of mineral dissolution developed. The highest benthic TA fluxes were generated during the dissolution of aragonite while the lowest values were produced in the low R_C^0 scenario (Figure 5D). Baseline and deeper bioturbation layer scenarios produced very similar results while high FeOx flux scenario produced slightly lower TA fluxes. Lowering overlying water pH led to decreases in saturation state and pH while increasing concentration and flux of alkalinity.
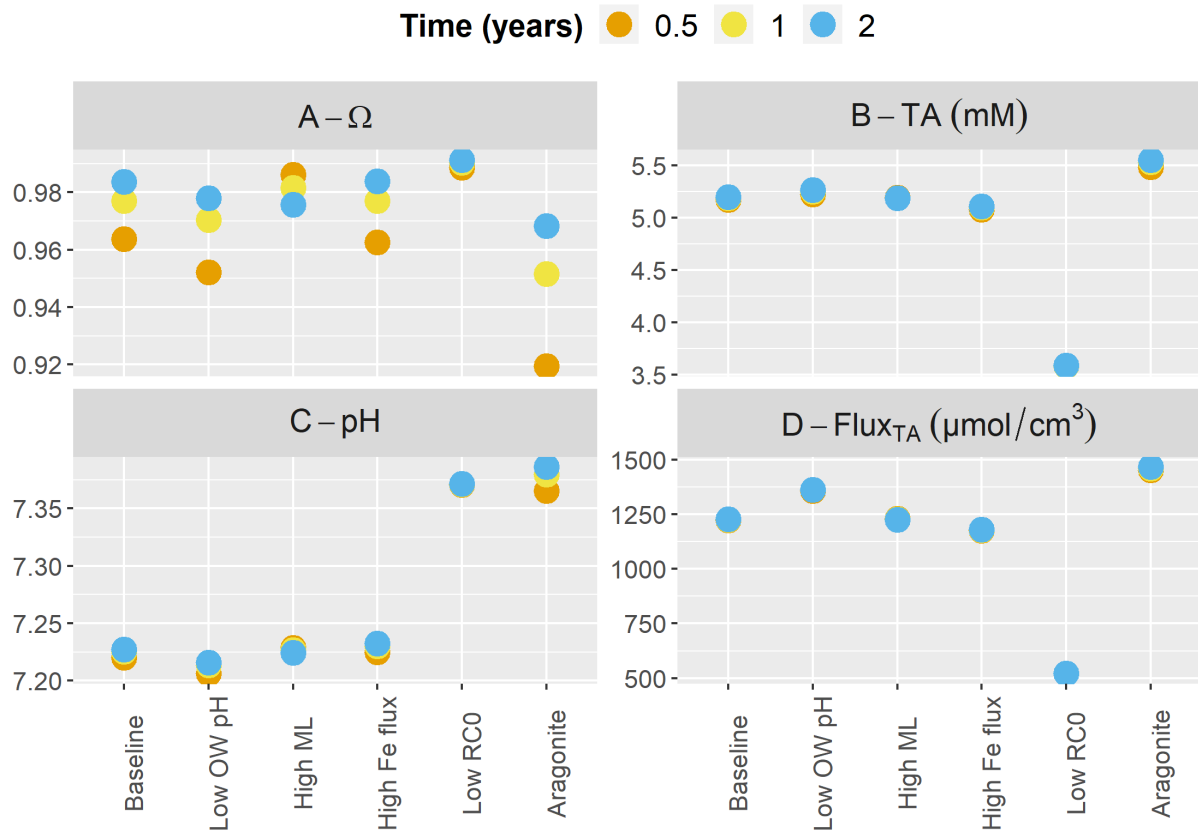
Figure 5. Buffering response after carbonate mineral additions for a range of environmental conditions. Concentrations are averaged over the top 10cm. Scenarios listed on the x axis (from left to right) represent: baseline simulation; baseline with lower overlying water pH representing ocean acidification scenario (7.8); baseline with deeper mixed layer (10 cm); baseline with higher Fe flux (10 μmol cm^{-2} yr^{1}); baseline with lower R_C^0 (200 μmol cm^{-3}); baseline with aragonite instead of calcite.

A lower pH in the overlying water that represents ocean acidification led to a lower pH in the porewater and less saturated conditions in surface sediments (Figure 5). This promoted mineral dissolution and therefore led to increased TA production and flux to the overlying water. This demonstrates the sensitivity of buffering towards the overlying water conditions. Deeper bioturbation led to faster downward mixing and subsequent dissolution of the added mineral which then led to rapid increase in TA, pH and saturation state (also seen in dpH/dTA, Figure S4). Higher mixing led to faster transport of minerals inducing enhanced dissolution in year 0.5 (i.e., Figure 5, higher buffering 0.5 than 2 years after mineral addition). However, faster transport extended the depth of buffering and diluted dissolution products, which caused a slight decrease in pH and saturation state after 2 years at the top 10 cm (Figure 5). Increased FeOx input to the sediment led to enhanced FeOx reduction which produced TA. However, increased reoxidation of Fe^{2+} led to decreased availability of O$_2$ and consumption of TA. This balanced

out the additional TA produced through FeOx reduction and led to an additional net consumption of ~46 µmol cm^{-2} yr^{-1} of TA. Overall, increased iron oxide supply led to slight decreases in TA concentrations and fluxes, and small increases in pH showing an effect similar to decreasing the OM mineralization rate (Figure 5). TA production and flux was significantly lower in low OM reaction rate scenario (Figure 5D) which showed the critical impact of OM mineralization on TA dynamics. The lower

400   rate of OM mineralization decreases TA production, both through the reduction of overall mineralization rates, and the reduction of the relative contribution of anaerobic mineralization pathways like dissimilatory sulfate reduction. The low rate of aerobic mineralization also led to reduced H$^+$ production, which in turn slows carbonate dissolution (Morse & MacKenzie, 1990). However, even with lower dissolution, this situation led to higher pH than the baseline suggesting that the artificial buffering might not be needed to maintain saturated conditions in environments where OM reactivity is low. In deeper layers

405   where the surficial mineral addition is not as effective, TA and mineral saturation states will be lower due to lower anaerobic TA production. Notably, the effect of changing the OM mineralization rate is not linear, and halving the rate reduced the benthic alkalinity flux by a factor of about 2.5. In our simulations, the lower OM mineralization rate led to depth-integrated reduction by 29% for aerobic mineralization, 19% for denitrification, 55% for sulfate reduction and 380% for mineral dissolution. Aside from the impact on the partitioning of OM mineralization between metabolic pathways, this mainly reflects

410   that changes in mineralization rates lead to differences in the porewater conditions, which in turn alter the rate of mineral dissolution/precipitation. Due to the higher solubility and hence larger degree of undersaturation, initial aragonite dissolution was faster than calcite. Hence, aragonite produced the largest TA in 2 years, generated highest benthic TA fluxes, and increased the pH the most. The addition of aragonite produced more buffering than the scenario with lower OM mineralization which shows the potential of artificial buffering overcoming the acidification impact due to OM mineralization.

415

3.3 Limitations and challenges

Our model demonstrates the potential for coastal sediment alkalinization to improve the biogeochemical conditions for juvenile calcifying organisms living in surficial sediments. However, alkalinity fluxes are sensitive to overlying water conditions, temporal changes in overlying water should be considered. These changes include the impact of short-term diel patterns and

420   small scale spatial heterogeneity on benthic fluxes (Gadeken et al., 2023), seasonal changes such as temperature (Rao et al., 2014) and long-term changes such as anthropogenic impacts (Pacella et al., 2018; e.g. eutrophication, Cai et al., 2011). In addition, in particular in near-shore shallow water environments, one may have to take into consideration the input of groundwater (Cyronak et al., 2013a), advective flow through sand ripples (Huettel et al., 1998) and other factors driving advective flow in marine sediments (Santos et al., 2012), which can impact sediment biogeochemistry and alkalinity fluxes.

425   Furthermore, the prediction of the time course of buffering by mineral dissolution may need to consider dissolution rate expressions that account for changes in mineral surface areas, rather than bulk concentrations (Morse et al., 2007), and the potential for washing away or enhancing dissolution (Meysman & Montserrat, 2017) of minerals deposited to the sediment in high-energy environments.

Our results indicate a lasting buffering effect of mineral additions. This finding depends on the kinetics of the mineral
430 dissolution rate, in particular the reaction order. Given the range of observations (Adkins et al., 2021; Subhas et al., 2018), the
temporal evolution of the dissolution rates in the field needs to be explored further. In addition, our model assumes that the
minerals are mixed into the upper 2 cm of sediment, matching recent field manipulation experiments in Yaquina Bay. However,
an important consideration is how the minerals are applied to the surface sediment. For example, a simple 'top-dressing'
approach would involve less disturbance to the sediment and less labor than surface raking, but may be washed away more
435 easily, and react less readily with the metabolic acids produced in the underlying sediment. Thus, optimal mineral application
and subsequent effects clearly requires field trials across a range of hydrodynamic settings

3.4 Potential impact of benthic fluxes on marine CO_2 uptake

Benthic alkalinity fluxes are critical for water column C dynamics especially in shallow water environments where water
column and atmospheric interactions are more sensitive to processes occurring in the sediment (Brenner et al., 2016). The
440 significant decrease in shells due to overharvesting has likely altered alkalinity cycling in estuarine waters, such as Chesapeake
Bay (Waldbusser et al., 2013). One outcome of this benthic-pelagic connection is the impact of benthic fluxes on oceanic CO_2
uptake which was estimated to have significant influence in the North Sea (Thomas et al., 2009), and the potential for shallow
water sediment alkalinization to alter overlying water.

We estimated the potential impact of enhanced sediment TA fluxes on atmospheric CO_2 uptake in Yaquina Bay, OR (USA)
445 using the diagenetic model output (baseline scenario) in a simple box model at the peak buffering period (~2 years after
addition). The bay was found to be net heterotrophic, with tidal exchange and net respiration in the water column impacting
air-sea CO_2 flux the most. The impact of sediment buffering on the air-sea CO_2 was estimated as the difference in atmospheric
CO_2 fluxes between before and after the mineral addition. Mineral addition resulted in a TA flux enhancement of ~126 µmol
cm^{-2} yr^{-1} and a decrease in CO_2 flux by approximately 58 µmol cm^{-2} yr^{-1}, which was comparable to previous studies (Brenner
450 et al., 2016). Scaling to a 10 m water depth (or per liter of water), this stoichiometrically estimated marine carbon dioxide
removal (mCDR) due to the application and subsequent dissolution of carbonate minerals by the sediments results in a similar
amount of mCDR as the current estimates of the anthropogenic C (C_{anth}) concentration in the US Pacific coast waters, 30-60
µmol L^{-1} (Feely et al. 2016, Pacella et al. 2024). It is important to note three key points in this estimate: (1) the uptake of C_{anth}
by marine waters from anthropogenic activities results in an increase of DIC without any concurrent change in alkalinity, thus
455 acidification. (2) alkalinity enhancement shifts the carbonate speciation and allows increased uptake of atmospheric CO_2 by
marine waters. Thus, ocean alkalinity enhancement increases the total amount of C_{anth} in seawater. However, while C_{anth} and
DIC both increase with OAE, (3) the mineral dissolution due to sediment respiration results in an increase in the TA:DIC ratio,
thus providing the mCDR benefit of atmospheric removal as well as mitigating existing acidification impacts. The annual
mCDR effect modelled here, while notable compared to the total anthropogenic impact, is however miniscule compared to the
460 total air-sea exchange flux, which is driven by tidal exchange of DIC and alkalinity between the bay and the coastal ocean and

biogeochemical processes in the water column. The signal to noise of this potentially significant effect also highlights the existing measurement challenges in accurately discerning OAE effects within coastal systems.

4. Conclusions

Our study successfully combines lab experiments and modeling to investigate the impact of coastal alkalinity enhancement, points to critical aspects to be considered and presents the potential of carbonate additions as a mitigation strategy for the effects of climate change in coastal settings. We demonstrated that addition of minerals increased pH and saturation state of the sediment over the timespan of a few months and had the potential to persist over 30-40 years after which subsequent additions might be needed to sustain buffering. During the peak buffering period, porewater in the top 10 cm of the sediment was almost fully saturated with respect to the mineral added, which implies favorable conditions for benthic calcifying organisms. We showed that two main pathways of producing TA in the sediment were sulfate reduction and mineral dissolution with sulfate reduction having a larger impact. We also demonstrated that the type of mineral was an important factor affecting benthic fluxes and that the application of an increased amount of minerals was effective in extending the duration rather than the strength of the buffering.

Our analysis suggests that buffering through mineral additions to coastal sediments can establish biogeochemical conditions that are conducive for the growth and development of calcifying benthic organisms. However, the effect of mineral additions can vary substantially between environments. Sensitivity analyses demonstrated that the OM mineralization had a significant impact on mineral dissolution, pH and mineral saturation. The type of mineral added also showed significant effect with aragonite producing more TA and higher pH. Increased mixing depth led to a faster increase in saturation state while increased iron flux caused reduction in TA concentration and benthic fluxes. Overall, the addition of minerals with higher dissolution rates would be most effective especially in environments with high OM degradation and undersaturated water conditions. Similarly, the type of mineral and the environmental conditions affect mCDR potential through benthic fluxes. Importantly, the implementation of OAE can lead to unforeseen effects, including ecological feedback such as changes in species composition (Bach et al., 2019; Köhler et al., 2013), and the effectiveness of carbonate additions may depend strongly on site characteristics. Thus, studies should combine field, lab and modeling components (Meysman & Montserrat, 2017) to improve predictive capabilities and decrease uncertainty.

Code Availability

The reaction transport model can be found at: https://bitbucket.org/MeileLab/kadir_oa/src/master/

Data Availability

Data for this manuscript is available in Myers (2022).

Author contribution

Lab experiments were designed by GW and TM, carried out by TM with the guidance of GW. KB developed the numerical model with guidance of CM and carried out the simulations. KB prepared the initial draft of the manuscript with significant input from CM, TM and GW.

495 **Competing interests**

The authors declare that they have no conflict of interest.

Acknowledgements

The authors would like to thank the ClimateWorks Foundation for funding and Jurjen Rooze for input on the model implementation.

500 **References**

Adkins, J. F., Naviaux, J. D., Subhas, A. V., Dong, S., & Berelson, W. M. (2021). The dissolution rate of $CaCO_3$ in the ocean. Annual Review of Marine Science, 13(1), 57-80.

Aller, R. C. (1982). The effects of macrobenthos on chemical properties of marine sediment and overlying water. In Animal-sediment relations: the biogenic alteration of sediments (pp. 53-102). Boston, MA: Springer US.

505 D'Andrea, A. F., & DeWitt, T. H. (2009). Geochemical ecosystem engineering by the mud shrimp Upogebia pugettensis (Crustacea: Thalassinidae) in Yaquina Bay, Oregon: Density-dependent effects on organic matter remineralization and nutrient cycling. Limnology and Oceanography, 54(6), 1911-1932.

Bach, L. T., Gill, S. J., Rickaby, R. E., Gore, S., & Renforth, P. (2019). CO_2 removal with enhanced weathering and ocean alkalinity enhancement: potential risks and co-benefits for marine pelagic ecosystems. Frontiers in Climate, 1, 7.

510 Bandstra, L., Hales, B., & Takahashi, T. (2006). High-frequency measurements of total CO_2: Method development and first oceanographic observations. Marine Chemistry, 100(1-2), 24-38.

Barton, A., Hales, B., Waldbusser, G. G., Langdon, C., & Feely, R. A. (2012). The Pacific oyster, Crassostrea gigas, shows negative correlation to naturally elevated carbon dioxide levels: Implications for near-term ocean acidification effects. Limnology and oceanography, 57(3), 698-710.

515 Berelson, W. M., Balch, W. M., Najjar, R., Feely, R. A., Sabine, C., & Lee, K. (2007). Relating estimates of $CaCO_3$ production, export, and dissolution in the water column to measurements of $CaCO_3$ rain into sediment traps and dissolution on the sea floor: A revised global carbonate budget. Global Biogeochemical Cycles, 21(1).

Berner, R. A. (1980). Early diagenesis: a theoretical approach. 241 p. Princeton University Press.

Boudreau, B. P. (1984). On the equivalence of nonlocal and radial-diffusion models for porewater irrigation. Journal of Marine
520 Research, 42(3), 731-735.

Boudreau, B. P. (1996). The diffusive tortuosity of fine-grained unlithified sediments. Geochimica et Cosmochimica Acta, 60(16), 3139-3142.

Boudreau, B. P. (1997). Diagenetic models and their implementation. 414 p. (Vol. 505). Berlin: Springer.

Brenner, H., Braeckman, U., Le Guitton, M., & Meysman, F. J. (2016). The impact of sedimentary alkalinity release on the
525 water column CO_2 system in the North Sea. Biogeosciences, 13(3), 841-863.

Burdige, D. J. (2007). Preservation of organic matter in marine sediments: controls, mechanisms, and an imbalance in sediment organic carbon budgets? Chemical Reviews, 107(2), 467-485.

Burdige, D. J., Hu, X., & Zimmerman, R. C. (2010). The widespread occurrence of coupled carbonate dissolution/reprecipitation in surface sediments on the Bahamas Bank. *A*merican Journal of Science, 310(6), 492-521.

Cai, W. J., Hu, X., Huang, W. J., Murrell, M. C., Lehrter, J. C., Lohrenz, S. E., ... & Gong, G. C. (2011). Acidification of subsurface coastal waters enhanced by eutrophication. Nature geoscience, 4(11), 766-770.

Cai, W. J., Huang, W. J., Luther III, G. W., Pierrot, D., Li, M., Testa, J., ... & Kemp, W. M. (2017). Redox reactions and weak buffering capacity lead to acidification in the Chesapeake Bay. Nature Communications, 8(1), 369.

Cyronak, T., Santos, I. R., Erler, D. V., & Eyre, B. D. (2013a). Groundwater and porewater as major sources of alkalinity to a fringing coral reef lagoon (Muri Lagoon, Cook Islands). Biogeosciences, 10(4), 2467-2480.

Cyronak, T., Santos, I. R., McMahon, A., & Eyre, B. D. (2013b). Carbon cycling hysteresis in permeable carbonate sands over a diel cycle: Implications for ocean acidification. Limnology and Oceanography, 58(1), 131-143.

Dickson, A. G. (1981). An exact definition of total alkalinity and a procedure for the estimation of alkalinity and total inorganic carbon from titration data. Deep Sea Research Part A. Oceanographic Research Papers, 28(6), 609-623.

Dickson, A. G. (1990). Standard potential of the reaction: AgCl (s)+ 12H2 (g)= Ag (s)+ HCl (aq), and and the standard acidity constant of the ion HSO4− in synthetic sea water from 273.15 to 318.15 K. *The Journal of Chemical Thermodynamics*, *22*(2), 113-127.

Edmond, J. M., & Gieskes, J. M. T. M. (1970). On the calculation of the degree of saturation of sea water with respect to calcium carbonate under in situ conditions. Geochimica et cosmochimica acta, 34(12), 1261-1291.

Egleston, E. S., Sabine, C. L., & Morel, F. M. (2010). Revelle revisited: Buffer factors that quantify the response of ocean chemistry to changes in DIC and alkalinity. Global Biogeochemical Cycles, 24(1).

Feely, R. A., Alin, S. R., Carter, B., Bednaršek, N., Hales, B., Chan, F., ... & Juranek, L. (2016). Chemical and biological impacts of ocean acidification along the west coast of North America. Estuarine, Coastal and Shelf Science, 183, 260-270.

Fuhr, M., Wallmann, K., Dale, A. W., Kalapurakkal, H. T., Schmidt, M., Sommer, S., ... & Geilert, S. (2024). Alkaline mineral addition to anoxic to hypoxic Baltic Sea sediments as a potentially efficient CO_2-removal technique. Frontiers in Climate, 6, 1338556.

Gadeken, K. J., Lockridge, G., & Dorgan, K. M. (2023). An in situ benthic chamber system for improved temporal and spatial resolution measurement of sediment oxygen demand. Limnology and Oceanography: Methods, *21*(11), 645-655.

Gimenez, I., Waldbusser, G. G., & Hales, B. (2018). Ocean acidification stress index for shellfish (OASIS): Linking Pacific oyster larval survival and exposure to variable carbonate chemistry regimes. Elem Sci Anth, 6, 51.

Goldenberg, S. U., Riebesell, U., Brüggemann, D., Börner, G., Sswat, M., Folkvord, A., ... & Moyano, M. (2024). Viability of coastal fish larvae under ocean alkalinity enhancement: from organisms to communities. EGUsphere.

Green, M. A., Waldbusser, G. G., Hubazc, L., Cathcart, E., & Hall, J. (2013). Carbonate mineral saturation state as the recruitment cue for settling bivalves in marine muds. Estuaries and Coasts, 36, 18-27.

560   Green, M. A., Waldbusser, G. G., Reilly, S. L., Emerson, K., & O'Donnell, S. (2009). Death by dissolution: sediment saturation state as a mortality factor for juvenile bivalves. Limnology and Oceanography, 54(4), 1037-1047.

Gustafsson, E., Hagens, M., Sun, X., Reed, D. C., Humborg, C., Slomp, C. P., & Gustafsson, B. G. (2019). Sedimentary alkalinity generation and long-term alkalinity development in the Baltic Sea. Biogeosciences, 16(2), 437-456.

Hales, B., Suhrbier, A., Waldbusser, G. G., Feely, R. A., & Newton, J. A. (2017). The carbonate chemistry of the "fattening
565   line," Willapa Bay, 2011–2014. Estuaries and Coasts, 40, 173-186.

Hales, B., Takahashi, T., & Bandstra, L. (2005). Atmospheric CO_2 uptake by a coastal upwelling system. Global Biogeochemical Cycles, 19(1).

Hangx, S. J., & Spiers, C. J. (2009). Coastal spreading of olivine to control atmospheric CO_2 concentrations: A critical analysis of viability. International Journal of Greenhouse Gas Control, 3(6), 757-767.

570   Hartmann, J., West, A. J., Renforth, P., Köhler, P., De La Rocha, C. L., Wolf-Gladrow, D. A., ... & Scheffran, J. (2013). Enhanced chemical weathering as a geoengineering strategy to reduce atmospheric carbon dioxide, supply nutrients, and mitigate ocean acidification. Reviews of Geophysics, 51(2), 113-149.

Hofmann, G. E., Smith, J. E., Johnson, K. S., Send, U., Levin, L. A., Micheli, F., ... & Martz, T. R. (2011). High-frequency dynamics of ocean pH: a multi-ecosystem comparison. PloS One, 6(12), e28983.

575   Hofmann, A. F., Soetaert, K., Middelburg, J. J., & Meysman, F. J. (2010). AquaEnv: An Aquatic Acid–Base Modelling Environment in R. Aquatic Geochemistry, 16, 507-546.

Hu, X., & Cai, W. J. (2011a). An assessment of ocean margin anaerobic processes on oceanic alkalinity budget. Global Biogeochemical Cycles, 25(3).

Hu, X., & Cai, W. J. (2011b). The impact of denitrification on the atmospheric CO_2 uptake potential of seawater. Marine
580   Chemistry, 127(1-4), 192-198.

Huettel, M., Ziebis, W., Forster, S., & Luther Iii, G. W. (1998). Advective transport affecting metal and nutrient distributions and interfacial fluxes in permeable sediments. Geochimica et Cosmochimica Acta, 62(4), 613-631.

Jahnke, R. A., Craven, D. B., & Gaillard, J. F. (1994). The influence of organic matter diagenesis on $CaCO_3$ dissolution at the deep-sea floor. Geochimica et Cosmochimica Acta, 58(13), 2799-2809.

585   Jourabchi, P., Meile, C., Pasion, L. R., & Van Cappellen, P. (2008). Quantitative interpretation of pore water O_2 and pH distributions in deep-sea sediments. Geochimica et Cosmochimica Acta, 72(5), 1350-1364.

Jourabchi, P., Van Cappellen, P., & Regnier, P. (2005). Quantitative interpretation of pH distributions in aquatic sediments: A reaction-transport modeling approach. American Journal of Science, 305(9), 919-956.

Köhler, P., Abrams, J. F., Völker, C., Hauck, J., & Wolf-Gladrow, D. A. (2013). Geoengineering impact of open ocean
590   dissolution of olivine on atmospheric CO_2, surface ocean pH and marine biology. Environmental Research Letters, 8(1), 014009.

Krumins, V., Gehlen, M., Arndt, S., Van Cappellen, P., & Regnier, P. (2013). Dissolved inorganic carbon and alkalinity fluxes from coastal marine sediments: model estimates for different shelf environments and sensitivity to global change. Biogeosciences, 10(1), 371-398.

595 Luff, R., & Wallmann, K. (2003). Fluid flow, methane fluxes, carbonate precipitation and biogeochemical turnover in gas hydrate-bearing sediments at Hydrate Ridge, Cascadia Margin: numerical modeling and mass balances. Geochimica et Cosmochimica Acta, 67(18), 3403-3421.

Meile, C., & Cappellen, P. V. (2003). Global estimates of enhanced solute transport in marine sediments. Limnology and Oceanography, 48(2), 777-786.

600 Meysman, F. J., & Montserrat, F. (2017). Negative CO2 emissions via enhanced silicate weathering in coastal environments. Biology Letters, 13(4), 20160905.

Middelburg, J. J., Soetaert, K., & Herman, P. M. (1997). Empirical relationships for use in global diagenetic models. Deep Sea Research Part I: Oceanographic Research Papers, 44(2), 327-344.

Middelburg, J. J., Soetaert, K., Herman, P. M., & Heip, C. H. (1996). Denitrification in marine sediments: A model study.
605 Global Biogeochemical Cycles, 10(4), 661-673.

Millero, F. J. (2010). Carbonate constants for estuarine waters. Marine and Freshwater Research, 61(2), 139-142.

Montserrat, F., Renforth, P., Hartmann, J., Leermakers, M., Knops, P., & Meysman, F. J. (2017). Olivine dissolution in seawater: implications for CO_2 sequestration through enhanced weathering in coastal environments. Environmental Science & Technology, 51(7), 3960-3972.

610 Morris, A. W., & Riley, J. P. (1966, August). The bromide/chlorinity and sulphate/chlorinity ratio in sea water. In *Deep sea research and oceanographic Abstracts* (Vol. 13, No. 4, pp. 699-705). Elsevier.

Morse, J. W., Arvidson, R. S., & Lüttge, A. (2007). Calcium carbonate formation and dissolution. Chemical Reviews, 107(2), 342-381.

Morse, J. W., & Mackenzie, F. T. (1990). Geochemistry of sedimentary carbonates. Elsevier.

615 Mucci, A. (1983). The solubility of calcite and aragonite in seawater at various salinities, temperatures, and one atmosphere total pressure. American Journal of Science, 283(7), 780-799.

Mucci, A., Sundby, B., Gehlen, M., Arakaki, T., Zhong, S., & Silverberg, N. (2000). The fate of carbon in continental shelf sediments of eastern Canada: a case study. Deep Sea Research Part II: Topical Studies in Oceanography, 47(3-4), 733-760.

Myers, T. J. (2022). Buffering Estuarine Sediments Against Acidification. Master's Thesis. 77p. Oregon State University.
620 https://ir.library.oregonstate.edu/concern/graduate_thesis_or_dissertations/br86bb964

Pacella, S. R., Brown, C. A., Labiosa, R. G., Hales, B., Mochon Collura, T. C., Evans, W., & Waldbusser, G. G. (2024). Feedbacks between estuarine metabolism and anthropogenic CO_2 accelerate local rates of ocean acidification and hasten threshold exceedances. Journal of Geophysical Research: Oceans, 129(3), e2023JC020313.

Pacella, S. R., Brown, C. A., Waldbusser, G. G., Labiosa, R. G., & Hales, B. (2018). Seagrass habitat metabolism increases
625   short-term extremes and long-term offset of CO_2 under future ocean acidification. Proceedings of the National Academy of
Sciences, 115(15), 3870-3875.

Paul, A. J., Haunost, M., Goldenberg, S. U., Hartmann, J., Sanchez, N. S., Schneider, J., ... & Riebesell, U. (2024). Ocean
alkalinity enhancement in an open ocean ecosystem: Biogeochemical responses and carbon storage durability. EGUsphere.

Rao, A. M., Malkin, S. Y., Montserrat, F., & Meysman, F. J. (2014). Alkalinity production in intertidal sands intensified by
630   lugworm bioirrigation. Estuarine, Coastal and Shelf Science, 148, 36-47.

Rassmann, J., Lansard, B., Pozzato, L., & Rabouille, C. (2016). Carbonate chemistry in sediment porewaters of the Rhône
River delta driven by early diagenesis (northwestern Mediterranean). Biogeosciences, 13(18), 5379-5394.

Renforth, P., & Henderson, G. (2017). Assessing ocean alkalinity for carbon sequestration. Reviews of Geophysics, 55(3),
636-674.

635   Riley, J. P. (1965). The occurrence of anomalously high fluoride concentrations in the North Atlantic. *Deep Sea Research
A*, *12*(2), 219-220.

Rooze, J., Egger, M., Tsandev, I., & Slomp, C. P. (2016). Iron-dependent anaerobic oxidation of methane in coastal surface
sediments: Potential controls and impact. Limnology and Oceanography, 61(S1), S267-S282.

Rooze, J., Peterson, L., Peterson, R. N., & Meile, C. (2020). Porewater flow patterns in surficial cold seep sediments inferred
640   from conservative tracer profiles and early diagenetic modeling. Chemical Geology, 536, 119468.

Santos, I. R., Eyre, B. D., & Huettel, M. (2012). The driving forces of porewater and groundwater flow in permeable coastal
sediments: A review. Estuarine, Coastal and Shelf Science, 98, 1-15.

Soetaert, K., Herman, P. M., & Middelburg, J. J. (1996). A model of early diagenetic processes from the shelf to abyssal
depths. *Geochimica et Cosmochimica Acta*, *60*(6), 1019-1040.

645   Soetaert, K., Hofmann, A. F., Middelburg, J. J., Meysman, F. J., & Greenwood, J. (2007). The effect of biogeochemical
processes on pH. Marine Chemistry, 106(1-2), 380-401.

Soetaert, K., Petzoldt, T., & Meysman, F. (2010). Marelac: Tools for aquatic sciences. https://cran.r-project.org/package=marelac

Subhas, A. V., Rollins, N. E., Berelson, W. M., Erez, J., Ziveri, P., Langer, G., & Adkins, J. F. (2018). The dissolution behavior
650   of biogenic calcites in seawater and a possible role for magnesium and organic carbon. Marine Chemistry, 205, 100-112.

Taylor, L. L., Quirk, J., Thorley, R. M., Kharecha, P. A., Hansen, J., Ridgwell, A., ... & Beerling, D. J. (2016). Enhanced
weathering strategies for stabilizing climate and averting ocean acidification. Nature Climate Change, 6(4), 402-406.

Thamdrup, B., & Canfield, D. E. (2000). Benthic respiration in aquatic sediments. In Methods in Ecosystem Science (pp. 86-103). New York, NY: Springer New York.

655   Thomas, H., Schiettecatte, L. S., Suykens, K. O. N. E., Koné, Y. J. M., Shadwick, E. H., Prowe, A. F., ... & Borges, A. V.
(2009). Enhanced ocean carbon storage from anaerobic alkalinity generation in coastal sediments. Biogeosciences, 6(2), 267-274.

Thullner, M., Dale, A. W., & Regnier, P. (2009). Global-scale quantification of mineralization pathways in marine sediments: A reaction-transport modeling approach. Geochemistry, geophysics, geosystems, 10(10).

660 Uppström, L. R. (1974). The boron/chlorinity ratio of deep-sea water from the Pacific Ocean. *Deep Sea Research A*, *21*(2), 161-162.

Waldbusser, G. G., Bergschneider, H., & Green, M. A. (2010). Size-dependent pH effect on calcification in post-larval hard clam Mercenaria spp. Marine Ecology Progress Series, 417, 171-182.

Waldbusser, G. G., Powell, E. N., & Mann, R. (2013). Ecosystem effects of shell aggregations and cycling in coastal waters: 665 an example of Chesapeake Bay oyster reefs. Ecology, 94(4), 895-903.

Waldbusser, G. G., & Salisbury, J. E. (2014). Ocean acidification in the coastal zone from an organism's perspective: multiple system parameters, frequency domains, and habitats. Annual Review of Marine Science, 6, 221-247.

Waldbusser, G. G., Steenson, R. A., & Green, M. A. (2011). Oyster shell dissolution rates in estuarine waters: effects of pH and shell legacy. Journal of Shellfish Research, 30(3), 659-669.

670 Wang, Y., & Van Cappellen, P. (1996). A multicomponent reactive transport model of early diagenesis: Application to redox cycling in coastal marine sediments. Geochimica et Cosmochimica Acta, 60(16), 2993-3014.

Wolf-Gladrow D.A., Zeeber, R.E., Klaas, C., Koertzinger, A. and Dickson, A.G. (2007). Total alkalinity: The explicit conservative expression and its application to biogeochemical processes. Marine Chemistry, 106, 287-300.

Zeebe, R. E., & Wolf-Gladrow, D. (2001). CO_2 in seawater: equilibrium, kinetics, isotopes (No. 65). Gulf Professional 675 Publishing.